Journal of ELECTRONIC MATERIALS, Vol. 48, No. 9, 2019
https://doi.org/10.1007/s11664-019-07372-7

Deposition and Electrical and Structural Properties of $La_{0.6}Sr_{0.4}CoO_3$ Thin Films for Application in High-Temperature Electrochemical Cells

BARTOSZ KAMECKI,[1] JAKUB KARCZEWSKI,[1] HAMID ABDOLI,[2] MING CHEN,[3] GRZEGORZ JASIŃSKI,[4] PIOTR JASIŃSKI,[4] and SEBASTIAN MOLIN [4,5]

1.—Faculty of Applied Physics and Mathematics, Gdańsk University of Technology, ul. G. Narutowicza 11/12, 80-233 Gdańsk, Poland. 2.—Department of Renewable Energy, Niroo Research Institute, End of Dadman Blv., Shahrak Ghods, P.O. Box: 1468613113, Tehran, Iran. 3.—Department of Energy Conversion and Storage, Technical University of Denmark, Risø Campus, Frederiksborgvej 399, 4000 Roskilde, Denmark. 4.—Faculty of Electronics, Telecommunications and Informatics, Gdańsk University of Technology, ul. G. Narutowicza 11/12, 80-233 Gdańsk, Poland. 5.—e-mail: sebastian.molin@pg.edu.pl

Low-temperature deposition of electroceramic thin films allows the construction of new devices and their integration with existing large-scale fabrication methods. Developing a suitable low-cost deposition method is important to further advance the development of microdevices. In this work, we deposited a 1-μm-thick $La_{0.6}Sr_{0.4}CoO_{3-\delta}$ (LSC) perovskite with high electrical conductivity on sapphire substrates at 400°C and analyzed its electrical, morphological and structural properties as a function of temperature in the range of 400–1100°C. The results show that spray pyrolysis can be used to deposit high-quality reproducible layers with the desired chemical and phase composition. Upon heating to around 600°C, the residual C–O and C=O species are removed, and the deposited layers crystallize and become conducting. The dependence of electrical conductivity versus processing temperature has a complex character—the maximum conductivity is found for layers processed at 800°C. An analytical model of stress distribution was used to predict stress to which the bi-layer material would be exposed to while being cooled down from the annealing temperature to room temperature. The high electronic conductivity and high-quality microstructure of the LSC layers, which can be adjusted with the appropriate heat treatment procedure, make them suitable for applications in electrochemical devices applied in integrated energy modules, including electrodes or contacts.

Key words: Thin film, spray pyrolysis, mixed electronic ionic conductor, electrical conductivity

INTRODUCTION

Mixed electronic-ionic conductors (MIEC) materials are the basic building blocks for many important devices: sensors, micro-mechanical systems, fuel cells and others.[1–5] Their integration into working devices depends on the availability of proper fabrication techniques. For applications in microelectromechanical systems (MEMS), active layers should be prepared at low temperatures to avoid the degradation of the other components, which can happen when sintering at high temperatures.[6–8] Spray pyrolysis is a versatile deposition method that is already used in the electronics industry,

(Received February 25, 2019; accepted June 11, 2019; published online June 27, 2019)

especially in the fabrication of gas sensors (direct integration with CMOS processes) and solar cells.[9,10] Unlike in the case of typical fabrication methods such as screen printing,[11] layers can be formed at temperatures that do not exceed 400°C.[12–14] Spray pyrolysis has been also studied as a possible method for the deposition of electrolytes and electrodes for miniaturized solid oxide fuel cells (SOFCs).[15–18] These fuel cells offer high energy conversion efficiency, and in some applications they can compete with Li-ion batteries.[16,19,20]

The performance of SOFCs at low temperatures is often described as being limited by a sluggish oxygen reduction reaction.[21–23] New materials are therefore being sought and improved fabrication methods (for example allowing nanocrystalline materials) are being developed.

Most oxygen electrode materials belong to the perovskite family.[24,25] The perovskite structure is described by a general formula ABO_3, where A and B are cations with a total charge of + 6. The larger A cation (e.g. La, Sr) with lower valence is coordinated to 12 oxygens, whereas the smaller B-site cation (e.g. Fe, Co, Ti) is coordinated to six oxygen atoms. In the case of charge deficiency (cation total charge < + 6), the difference is compensated by the formation of oxygen vacancies, and mixed ionic electronic conductors can thus be formed. Because there are many possibilities for selecting A and B cations, the multitude of perovskite materials can be studied.

Lanthanum-strontium cobaltite ($La_{1-x}Sr_xCoO_{3-\delta}$—LSC) perovskite is one of the most interesting oxygen electrode materials for use in solid oxide cells.[25–28] Its electronic structure with high electronic and ionic conductivities make it a very good oxygen reduction/oxidation catalyst for application in fuel cells and electrolytic cells.[29,30] One of its drawbacks is its high thermal expansion coefficient (TEC), which prevents its application at high temperatures due to thermal stresses arising between the components. The TEC of LSC has been reported to be $\sim 20.5 \times 10^{-6}$ K^{-1} in the temperature range of RT-800°C.[31] For comparison, TEC for the yttria-stabilized zirconia electrolyte is $\sim 10.8 \times 10^{-6}$ K^{-1} [32] and for c-plane sapphire it is $\sim 7.7 \times 10^{-6}$ K^{-1}. There is thus a very significant TEC difference between the materials.

The drive towards lowering the operating temperature of SOFCs has increased the intensity of research on LSC-based materials, their properties and applications in both fuel cells and electrolytic cells. In a study by Zhang-Steenwinkel et al.,[33] a state-of-the-art LSC oxygen electrode was used in an anode-supported cell with optimized diffusion barrier layers. This cell achieved a power density of 1 W cm^{-2} at 600°C, which can be considered an important milestone, since the cell employed an yttria-stabilized zirconia electrolyte, which is typically used at > 700°C. Other important applications of LSC include nanoelectrodes prepared via the impregnation of porous backbones/scaffolds using precursor solutions.[34,35] High-performance electrodes are produced by means of repetitive impregnation with intermediate heating. Since a relatively low heat treatment temperature (500–700°C) can be maintained, small grains of the infiltrated phase are formed, enhancing the effective length of triple phase boundaries available for the oxygen reduction reaction. Another approach to the fabrication of high-performance electrodes is the incorporation of a dense interfacial layer between the electrolyte and the porous electrode. This leads to very high performance of protonic and oxygen conducting cells[36–39] and seems to be a very promising approach with great potential. Developing a suitable deposition method that would provide microstructural and chemical control of the produced films is essential for making further improvements and obtaining more efficient electrochemical devices.

This work presents the fabrication of LSC thin layers on sapphire single crystals via low-temperature spray pyrolysis (~ 400°C). These layers can find applications in electrocatalysis as well as modern gas sensors, electronic conductors, memristors and fuel cells, which can be used as part of integrated energy modules. Deposition is followed by electrical characterization and post-mortem evaluation of structural and morphological features.

EXPERIMENTAL

Deposition of Films

The $(La_{0.6}Sr_{0.4})CoO_{3-\delta}$(LSC64) layers were prepared by spray pyrolysis on sapphire single crystal substrates (c-plane cut, dimensions $10 \times 10 \times 0.5$ mm^3, single side polished, AdvalueTech, USA). Prior to use substrates they were cleaned in acetone in an ultrasonic bath. Spray pyrolysis was performed using a commercial airbrush (Paasche VLS, USA) operated with compressed air (2 bars). The spraying distance to the hotplate was ~ 50 cm. In this setup the sprayed area was ca. 10 cm in diameter. The hot plate was heated to 390°C (controlled by a thermocouple mounted below the sample). The precursor solution was fed to the airbrush using a syringe pump (Ascor AP14, Poland). A dosing rate of 2.5 mL min^{-1} was used after prior optimization of the deposition parameters. The solutions were prepared by mixing liquid solutions of metal salts with the pre-determined cation content (by thermogravimetric analysis). Lanthanum, strontium and cobalt nitrate (POCH, Poland) solutions were used. Precursor solution was composed of 9:1 volume ratio of tetraethyleneglycol (4EG) and water (including the dissolved cations).

For the analysis of the thickness of the layer in the function of the sprayed precursor quantity, samples were prepared from 0.5 mL, 1 mL, 2 mL, and 10 mL solutions. For each type two samples

were prepared. For the subsequent characterization, samples were prepared using 10 mL of solutions. Ten samples were prepared for the detailed characterization. Two samples were used for the electrical conductivity study, whereas the remaining ones were used to prepare a set of samples with different thermal processing history. Samples were heat treated at 500°C, 600°C, 700°C, 800°C, 900°C, 1000°C and 1100°C for 2 h (heating rate: 3 K/min, cooling with furnace) for further analysis.

Electrical Conductivity

The direct current electrical characterization of the thin layers was conducted using the van der Pauw method. Square 10 × 10 × 0.5 mm sample was contacted at the corners by Pt wires attached by silver paste. Wires were connected to an automated measurement system: electrode multiplexer and a Keithley 2400 SourceMeter. The multiplexer changes the electrodes as required by the van der Pauw technique. System also checks for any possible thermovoltage occurrence by switching current directions. The constant current working mode was used with a current value of 0.1–1 mA depending on the resistance value. The measurement was performed in sequential temperature ramps. After each longer dwell (10 h), starting from 600°C, the temperature was lowered in steps by 50°C (15 min ramp) and held for 30 min at each temperature. After reaching 300°C the temperature was increased to reach 50°C before the previous maximum temperature.

Microstructural Characterization

The microstructure of the samples was analyzed by x-ray diffraction (XRD) using a Bruker D2 Phaser diffractometer with Lynxeye XE-T detector with $CuK_{\alpha 1}$ radiation (λ = 0.15406 nm). The Fourier transform infrared radiation (FT-IR) spectra were recorded using the attenuated total reflection (ATR) mode on a Perkin Elmer Frontier spectrophotometer with resolution of 2 cm^{-1} in the range of 4000–900 cm^{-1}. Samples were studied directly after the deposition and samples annealed at 500°C and 600°C. The morphology of the obtained samples was investigated by scanning electron microscopy (FEI Quanta FEG 250) with an ET (Everhart–Thornley) secondary electron detector at an acceleration voltage of 20 kV. For elemental analysis, the energy dispersive x-ray spectroscopy (EDS) was performed by EDAX Genesis APEX 2i with ApolloX SDD spectrometer. Atomic force microscopy (AFM) was performed using a Nanosurf Easy Scan 2 working in the contact mode.

Phase Diagram Calculation

A phase diagram of $AlO_{1.5}$-SrO was calculated using FACTSAGE Thermochemical Software and Databases.[40]

Bi-Axial Stress Calculation

The calculations were based on works by Hsueh[41,42] for an n-layered structure with composite material properties derived by averaging the material properties of each layer, weighted by layer thickness. Hsueh's model allows the layers to have individual thermo-elastic material properties. This formulation was chosen because it provides an exact solution for the stress in the substrate and coating layers from a set of closed form equations. In this calculation the free bottom surface of the sapphire substrate is located at $z = 0$ and the free top surface of LSC is located at $z = h_1 + h_2$ (thickness of the substrate + thickness of the layer). When the bi-layer is cooled down from the annealing temperature to room temperature, it experiences an unconstrained differential shrinkage due to the cooling temperature range (ΔT), such that thermal strains, $\alpha_1 \Delta T$ and $\alpha_2 \Delta T$ (α—thermal expansion coefficient), exist in the sapphire substrate and LSC layer, respectively. Uniform tensile/compressive residual stresses are evolved in the individual layers for displacement compatibility, such that the strain in the bi-layer is a constant, c, and the net force on the system remains zero. Bending of the hybrid structure in consequence occurs induced by asymmetric stresses in the system.

By decomposing the total strain in the bi-layer material into a uniform and a bending component, the in-plane biaxial stress distributions in the sapphire substrate and LSC coating, σ_1 and σ_2, are:[42]

$$\sigma_1 = E_1^*(\varepsilon - \alpha_1 \Delta T) \text{ for sapphire layer} \quad (1)$$

$$\sigma_2 = E_2^*(\varepsilon - \alpha_2 \Delta T) \text{ for LSC layer} \quad (2)$$

where ε—strain, $E^* = E/(1 - \nu)$ is the biaxial modulus, E and ν are Young's modulus and Poisson's ratio, respectively. Both σ_1 in the substrate and σ_2 in the above equations are functions of film thickness.

RESULTS AND DISCUSSION

Fabrication of Layers

Spray pyrolysis is a droplet deposition-based method. The film is built through a sequential deposition of droplets splashing on a heated surface. In order to cover the entire surface, air atomized droplets must randomly cover the whole area. It is interesting to study the thickness limits for this method, where the full coverage of the substrate will occur and uniform film build-up will start.

Figure 1 presents SEM images of sapphire surfaces with different amounts of precursor sprayed. For 0.5 mL (spraying time 12 min), roughly 88% of the surface is covered by the deposits (bright areas correspond to the insulating sapphire substrate—contrast used to calculate image coverage

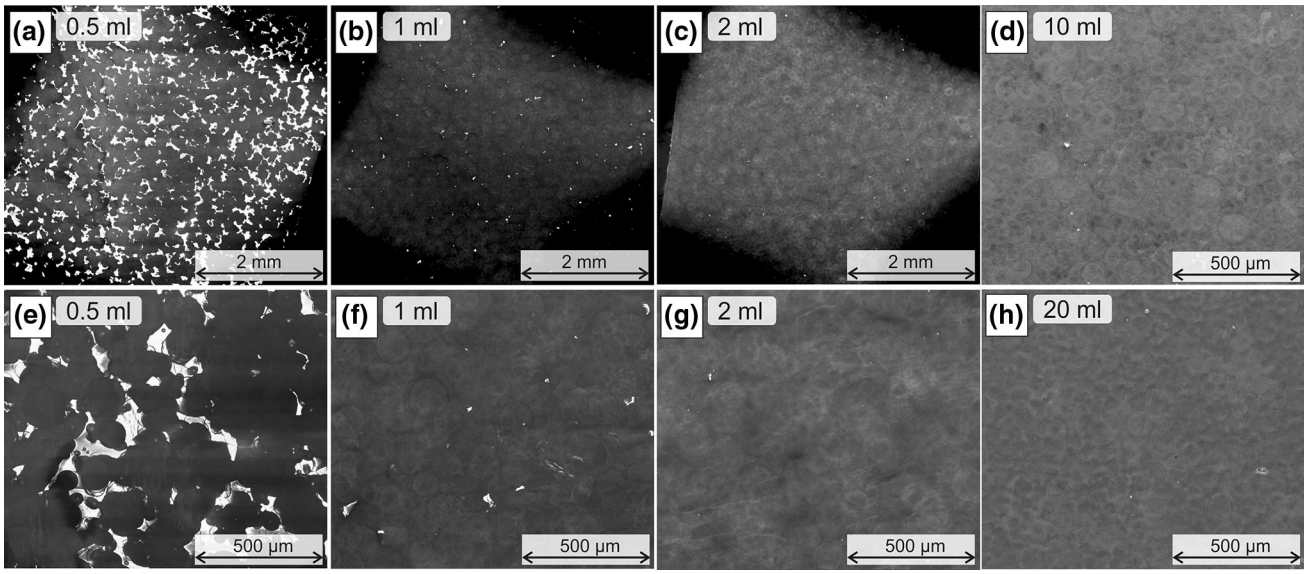

Fig. 1. SEM images of layers (surfaces) prepared with different amounts of precursors: 0.5 mL (a, e), 1 mL (b, f), 2 mL (c, g), 10 mL (d) and 20 mL (h).

percentages), whereas for 1 mL precursor > 98% of the surface is covered (spraying 24 min), but still, some small bright spots remain. When 2 mL of the solution is sprayed (spraying time 48 min), only a few small uncoated spots are noticed. For larger volumes (e.g. 10 mL, 20 mL) surface coverage is full with no substrate visible. From SEM analysis of the cross-sections (not shown here), the thickness for the 0.5 mL sample is ~ 50–100 nm, for the 1 mL it is 100 nm and for 2 mL the thickness is ~ 200 nm. Thicknesses of 1–2 μm are achieved for 10/20 mL of the spraying solution, so a linear scaling of the thickness versus the precursor amount seems to occur, as expected for a physical deposition process.

Through the years there has been discussion about the possible nature of the spray pyrolysis process—whether it is a physical vapor deposition (droplet) or chemical vapor deposition process. Based on the droplet pattern, clearly visible on the surface, at least the droplet delivery to the surface and its splashing can be considered a physical process. How exactly the splashed precursor transforms to the amorphous, crystalline-amorphous or crystalline deposit is not clear, nor is the aim of this work to resolve this. Potentially a local CVD process can be possible due to vaporization of the precursor. As has been presented, a proper deposition temperature to solvent boiling temperature ratio plays an important role. If the temperature is too high there will be no continuous film formation, and if the temperature is too low there will be too thick deposit that will shrink and form severely cracked layer.

In our study, the ratio of the solvent boiling temperature (328°C) to the deposition temperature (390°C) is 0.89 (in absolute temperatures), which agrees well with the range given by Beckel et al.[43]

In order to ensure full surface coverage and uniform coating for electrical characterization, samples with 10 mL precursor were prepared. This amount should result in layers with thicknesses ~ 1 μm.

ELECTRICAL CONDUCTIVITY STUDY

In order to determine the effect of heat treatments on the electrical properties of the prepared thin films, electrical conductivity study following a step-like behavior was carried out. During the first heating to 600°C, the sample increases its conductivity by several orders of magnitude. Previous studies revealed that up to 550°C, the sample has very a high resistance (not measurable in our setup). Above 550°C crystallization occurs, and the sample starts to conduct electrically to a measurable extent. This is visible in the first 5 h of the measurement. The electrical conductivity seems to reach maximum values after exposure to 800°C. After the temperature cycles, layer was cooled down to near room temperature (50°C). The electrical conductivity of LSC remained very high (~ 600 S cm^{-1}) even at room temperature (Fig. 2).

The longer (10 h) isothermal holds are plotted together in Fig. 3a and b. Monotonic increase of the electrical conductivity over the holding time is observed at temperatures from 600°C to 800°C. For temperatures 700°C, 750°C, and 800°C the extent of increase is quite similar. Above 800°C a decrease of electrical conductivity is observed. At 900°C the conductivity deteriorates much faster than at 850°C.

Using the data measured during cooling after each dwell, temperature dependence of electrical conductivity was plotted, as shown in Fig. 4a and b. The film processed at only 600°C exhibits a maximum of conductivity (~ 450°C). Higher processing temperatures lead to a monotonic increase in total

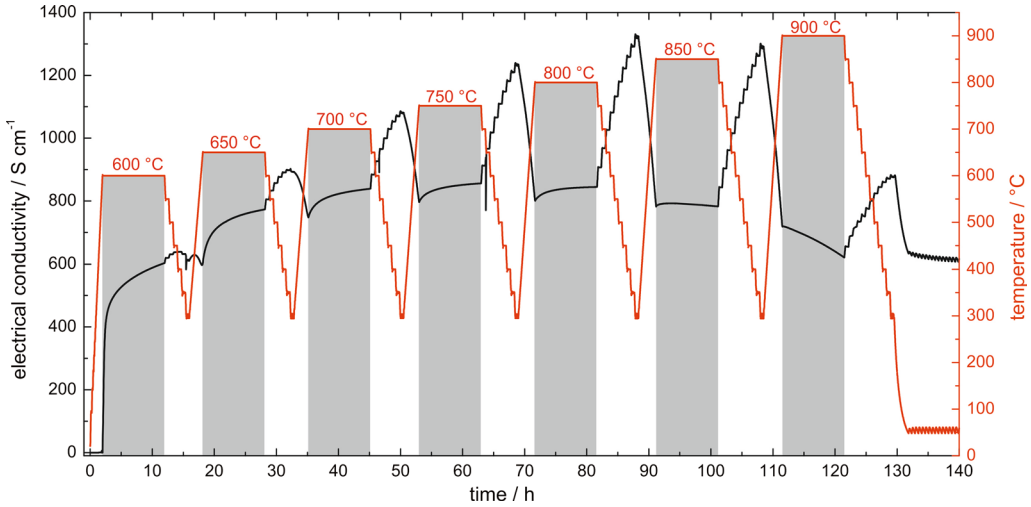

Fig. 2. Plot of the electrical conductivity values measured continuously in the programmed time–temperature sequence.

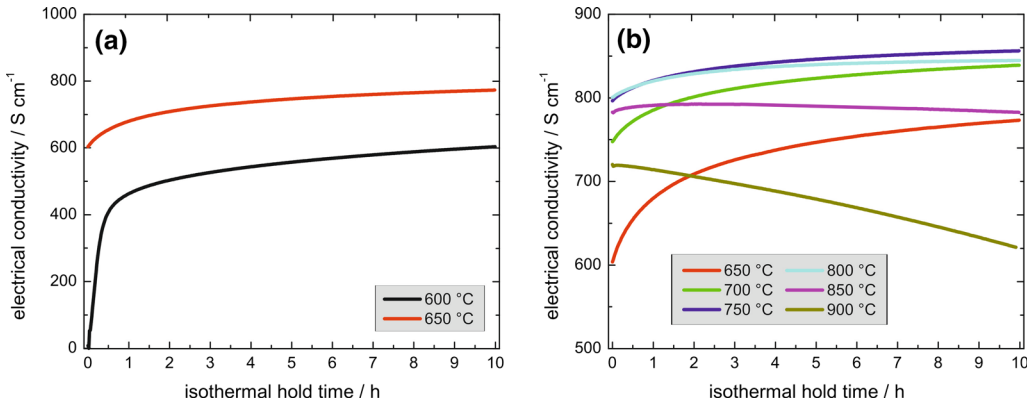

Fig. 3. Electrical conductivity of layers measured during the isothermal holds at different temperatures. Lower temperatures are presented separately (a) for clarity from higher temperatures (b).

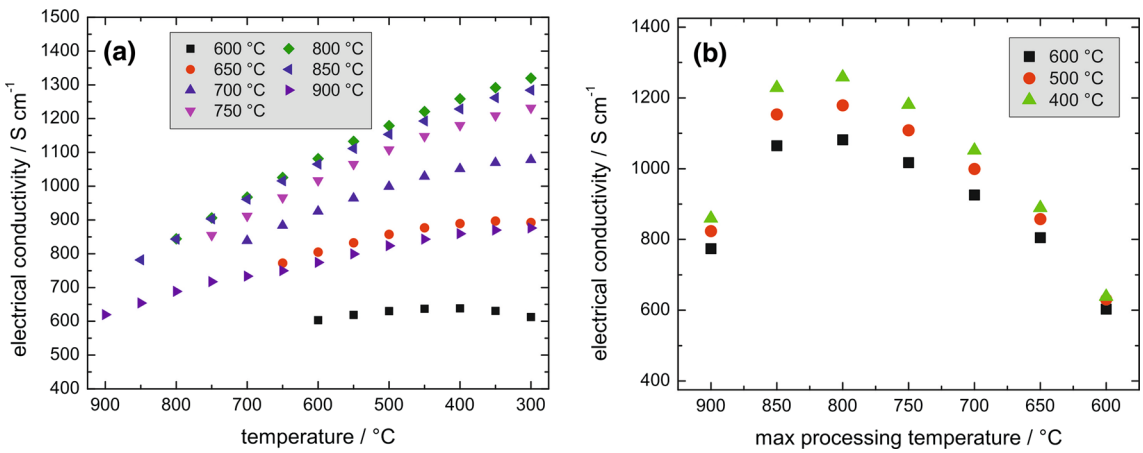

Fig. 4. Electrical conductivity values presented as a function of measurement temperature (a) and as a function of maximum processing temperature (b).

electronic conductivity and to metallic type behavior of conductivity as a function of temperature. The maximum electrical conductivity is reached after heat treatment at 800°C. In contrast to many other perovskites, electrical conductivity of LSC decreases with the increase of the temperature (metallic-like

behavior). This type of behavior has been described to be due to a decrease of the electron hole (charge carrier) concentration with an increasing temperature[25] and is characteristic for Sr content of 0.4, for materials with lower Sr content LSC shows a thermally activated electrical conductivity.[44]

The complex electrical conductivity dependence on the processing temperature might be caused by several competing processes. One mechanism might be based on the different contributions of grains and grain boundaries, as their relative fraction changes. At lower temperatures the grains are smaller, thus the relative fraction of the grain boundaries is higher. At higher temperatures, the grains are larger and the fraction of grain boundaries is lower. At higher temperature also formation of porosity due to grain growth might negatively influence the conductivity. Because of a large thermal expansion coefficient mismatch between the substrate and ceramic layer some cracking and delamination is also possible, though no large and rapid changes in the electrical conductivity plots were noticed. Mechanical issues are discussed in later parts. Another possibility that can cause changes in material properties is the possible surface segregation of Sr,[45] although that would be more visible in electrochemical measurements than in electrical conductivity measurements. In the case of thin films, where the Sr amount is limited, surface segregation might potentially change the inner composition. An interesting observation of surface recrystallization has been made by Tripković et al.[46] During work at intermediate temperatures, the surface exchange coefficient can decrease considerably. By annealing at higher temperatures the surface might come back to its initial properties. This recrystallization influenced only the electrochemical measurements, but is nonetheless an important and underestimated phenomenon. Finally, as discussed later in the manuscript, there is a chemical reaction between the LSC and sapphire, where the chemical composition change considerably, especially at temperatures $> 900°C$.

For comparison with other materials, Mosleh et al. have studied electrical conductivity of $La_{0.6}Sr_{0.4}FeO_3$ films on MgO substrates as a function of thickness.[47] The layers were produced by pulsed laser deposition. The total apparent conductivity of the layer was found to increase with increasing film thickness, approaching asymptotically the bulk values. It was noted that the thickness dependence of conductivity is caused by possible recrystallization and change of shape during heat treatment. In a series of studies of PLD deposited $La_xSr_{1-x}Co_yFe_{1-y}O_3$and $La_{0.85}Sr_{0.15}MnO_3$ layers by Płończak et al.,[48,49] the deposition parameters and heat treatment procedures played a key role on layers microstructure—porosity could be controlled by changing the atmosphere and temperature profiles. All these studies show a complex interplay between the chemical composition, phase and thermal history of the layers on their electrical and electrochemical response.

The effect of heat-treatment exposures on the isothermal electrical conductivity values is also presented in Fig. 4b. Electrical conductivity values at three different temperatures (measured at 400°C, 500°C, 600°C) are reported for differently exposed samples (values from the end of isothermal holds are used). Clearly a maximum is reached for the layers processed at 800°C. The difference in electrical conductivity between the layer processed at 600°C and 800°C is double the value (~ 600 S cm^{-1} at 600 C versus ~ 1300 S cm^{-1} at 800°C). Exposure at 900°C results in lowered electrical conductivity—decreases to the level previously obtained for the layer held at 650°C.

The maximum level of electrical conductivity measured in this work (1300 S cm^{-1}) is in good agreement with the reported values.[31] Ullmann et al. have reported electronic conductivity of 1500 S cm^{-1} and ionic conductivity as high as 0.22 S cm^{-1} at 800°C. Conductivity of bulk LSC64 in the form of sintered pellets was studied by Samat et al.[50] They studied the effect of sintering on electrical conductivity. Pellets sintered at 1200°C showed conductivity of 1500 S cm^{-1} at 500°C and presented a metallic-type conductivity. The values obtained in this work for layers annealed at 800°C are thus comparable to the values reported for bulk materials.

In order to describe the effect of different heat-treatments, microstructure of layers were analyzed after each processing step.

MICROSTRUCTURE OF SAMPLES

Sample surfaces were analyzed by SEM and AFM after different temperature exposures to determine the effects of temperature on grain growth, porosity formation etc. SEM images are presented in Fig. 5. Below 800°C the grains are very small and hard to differentiate clearly. At 800°C grains become clearly visible and grow with further temperature increase. At 1100°C a new phase can be observed, with large crystallites having an octahedral shape.

The surface of the layers after processing at temperatures $\leq 700°C$ seems to develop some surface "porosity". Large randomly distributed pores/cavities (diameter ~ 100 nm) are visible on the as-deposited sample and 600°C processed sample. At 700°C, the pore structure becomes uniform, cavities are distributed with similar spacing. At 800°C well crystallized grain structure with some surface porosity is found. The surface porosity seems to decrease for temperatures $> 800°C$ due to sintering of the layers.

In comparison to work by,[51] where LSC layers were deposited by PLD on YSZ and had many cracks after thermal treatment, no cracks were observed in our samples, even though a larger TEC

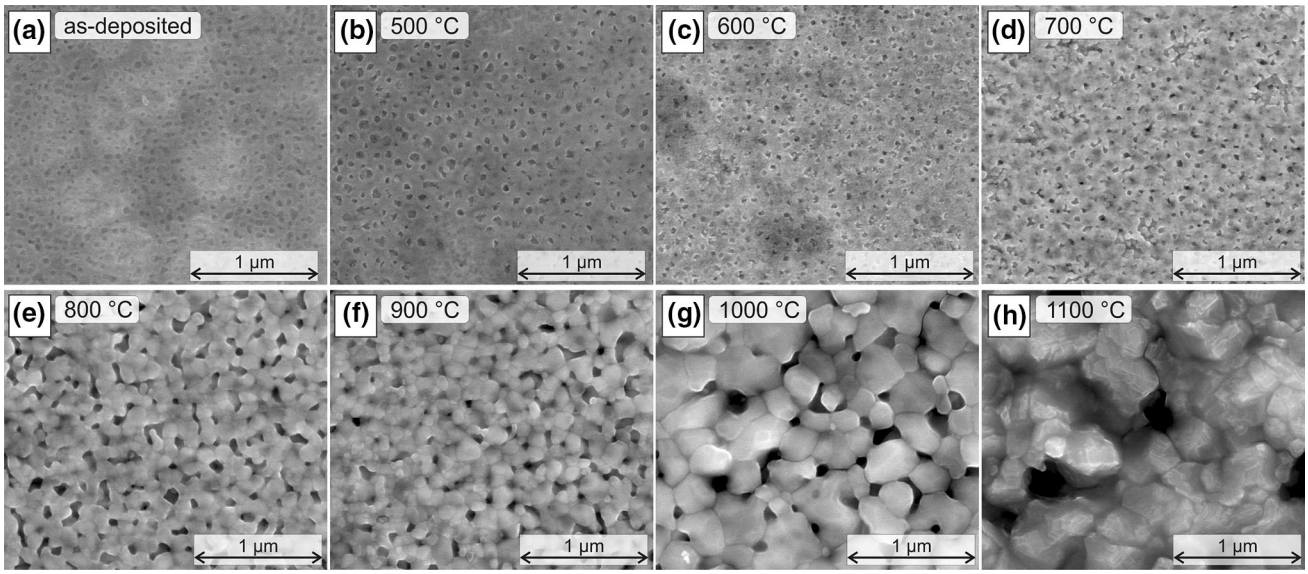

Fig. 5. SEM surface images of LSC layers on sapphire after different heat treatments: as-deposited (a), after: 500°C (b), 600°C (c), 700°C (d), 800°C (e), 900°C (f), 1000°C (g), 1100°C (h).

Table I. Chemical composition of the layers determined by EDS analysis of surfaces (at.%)

Composition/temperature:	a–d*	500°C	600°C	700°C	800°C	900°C	1000°C	1100°C
La	27.9	28.8	26.8	27.4	26.9	28.2	26.8	30.2
Sr	20	19.9	18.2	18.7	17.5	17.4	11.5	5.8
Co	45.9	47.3	43.9	45.4	43.9	46	42.9	27
Al	6.1	3.9	11.1	8.5	11.6	8.4	18.7	36.9
La/Sr	1.40	1.45	1.47	1.47	1.54	1.62	2.33	5.21
(La + Sr)/Co	1.04	1.03	1.03	1.01	1.01	0.99	0.89	1.33
Al/(La + Sr + Co)	0.065	0.041	0.125	0.093	0.131	0.092	0.230	0.586

*a–d as-deposited.

mismatch is present in our work (YSZ versus sapphire). Discussion about the thermal stresses generated due to TEC mismatch follow later in the text.

Chemical composition of the layers has been carried out with EDS on small magnification images (250×, scan area 500 × 500 μm^2). La, Co, Sr and Al cations were used in the calculations of the relative cation ratios. The measured values are presented in Table 1.

For temperatures lower than 900°C the measured lanthanum to strontium ratios are close to the desired ones (expected value = 1.5). Similarly, the A site to B site cations ratios are good (expected value = 1.0). In all measurements there is a clear signal from Al, coming from the sapphire substrate. For higher temperatures, starting from 900°C, strontium signal becomes less intense, suggesting its diffusion into the substrate. For 1000°C and 1100°C the signal from alumina has increased considerably, hinting towards possible interdiffusion of the layer with the substrate. As described in the literature, the LSC shows a tendency for Sr segregation by itself, which hinders its high electrochemical activity.[45,52] Further analyses were performed by analysis of cross-sections, as presented in later parts.

In order to analyze grain sizes in more detail, AFM analyses of surfaces were carried out and are presented in Fig. 6. Similarly to data obtained by SEM analysis, nice grain structure is observed for sample processed at ≤ 800°C. Grain size can be estimated to be 100–200 nm at 800°C. Increasing the temperature to 900°C does not lead to a visible grain growth. Exposure to 1000 C and 1100°C causes grain growth. Based on the AFM images, surface roughness parameter (S_a) and a real surface area to geometrical area ratio were calculated, values are given in Table 2.

Surface roughness increases monotonically with the increase of temperature. After deposition the films are smooth ($R_a \sim 1.6$ nm) and due to crystallization and grain formation and growth the roughness increases. Because of surface development, the

Table II. Surface roughness and area parameters

	a-d	500°C	600°C	700°C	800°C	900°C	1000°C	1100°C
R_a (S_a) [nm]	1.64	2.43	3.47	4.29	5.36	11.29	17.69	19.27
Surface area ratio (real/geometrical)	1.003	1.017	1.015	1.035	1.033	1.170	1.061	1.040

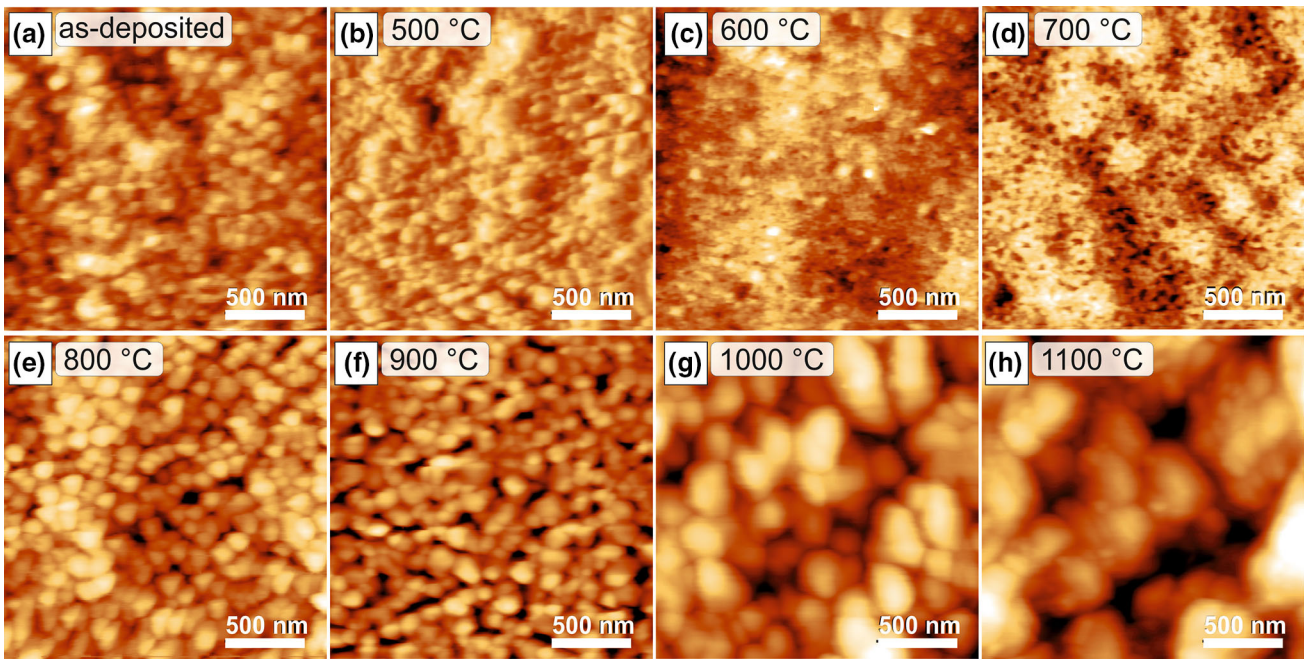

Fig. 6. AFM surface images of LSC layers on sapphire after different heat treatments: as-deposited (a), after: 500°C (b), 600°C (c), 700°C (d), 800°C (e), 900°C (f), 1000°C (g), 1100°C (h).

real surface area increases. The largest increase is found for the sample after 900°C; the real area is ~ 17% higher than the geometrical area of the substrate. Surface roughness and increase of the real area have important consequences in electrocatalysis, sensors and other applications, where interaction of the surface with the surrounding gas is important.

Studies of the development of the surface microstructures by SEM and AFM were complemented by x-ray diffractometry (XRD) and Fourier transform infrared radiation spectroscopy (FTIR).

XRD spectra measured after different heat treatments are presented in Fig. 7. Because of the small thickness of the ceramic film (~ 1 μm), the most intense peak in all spectra comes from the sapphire substrate (006 peak, $2\theta \sim 42.5$). For the sample processed at 900°C, the 003 peak from the sapphire is noticeable more than for the other samples, probably due to small misorientation of this particular substrate.

The spectra after the deposition and annealing at 500°C does not show peaks from the expected LSC perovskite phase. After annealing at 600°C, peaks from the perovskite become visible. In this work the rhombohedral structure is ascribed to the perovskite phase (according to #89-5719 card). Possibly also the cubic phase can be used for planes indexing (#89-5717). The precise determination of the phase is beyond the scope of the publication. Throughout the literature both phases have been used for description of the LSC materials. According to the LSC phase diagram presented by Petrov et al.,[44] LSC64 should have a rhombohedral structure at room temperature, that upon heating to higher temperature should transform into the cubic phase. Figure 7b presents the main peaks of the perovskite. The position of the peak corresponds well to the predicted 110 and 104 orientations. The splitting of the main peak into the two peaks is however not distinguishable.

The intensity of the perovskite phase increases with respect to the sapphire peaks intensity, with temperature increase. Also the peaks become narrower, suggesting crystallite size increase. Unit cell sizes were calculated assuming a pseudo-cubic

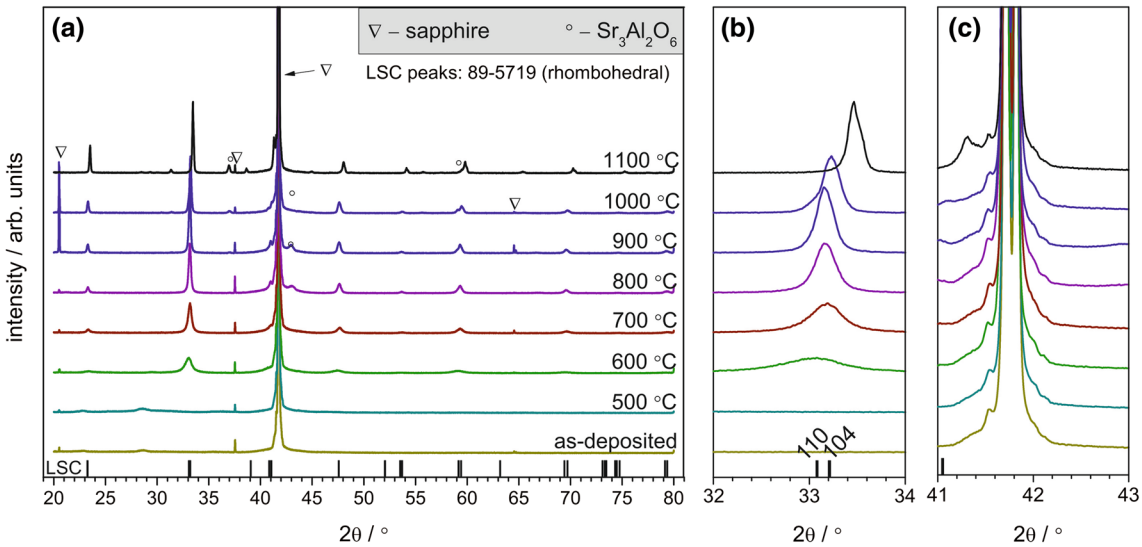

Fig. 7. XRD spectra of LSC layers on sapphire after different heat treatments: whole range (a) and selected smaller ranges (b, c) with main LSC or reaction peaks. The bottom ticks represent positions of peaks of the rhombohedral phase according to ICDD card #89-5719.

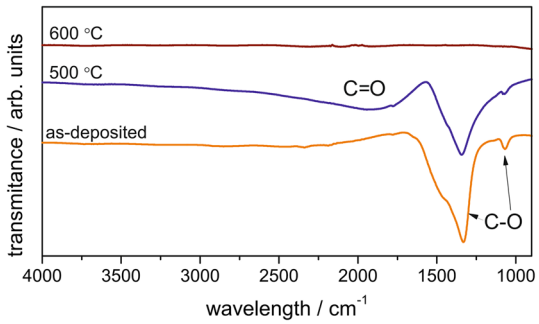

Fig. 8. FTIR spectra of coatings on sapphire after different heat treatments as-deposited, 500°C and °600 C.

structure from the position of the assumed 110 peak. For 600°C, the unit cell size was 3.933 Å, then for the increased temperatures the cell size becomes smaller (~ 3.981 Å at 700°C, 800°C, 900°C, ~ 3.975 Å at 1000°C and 3.951 Å at 1100°C). Comparing with literature data, Kubicek et al.[45] reported a pseudo-cubic cell parameter of 3.835 Å for PLD processed layers on YSZ, so smaller than the one reported here. Based on the spectra, it seems that secondary phases form after exposures to 800°C and higher. This is possibly the $Sr_3Al_2O_6$ phase (ICDD-JCPDS card #24-1187 or some other Sr-Al oxide: e.g. $Sr_3Al_{32}O_{51}$, card #2-964), as described by peak position (peaks at 2θ = 31.405° and 42.98°). Though the peak at 42.98° disappears for sample processed at 1100°C, maybe due to preferential orientation during reaction with monocrystalline sapphire. When more severe reaction occurs at 1100°C, as evidenced by more intense Sr-Al-O peaks, clear 110 peak shift occurs towards lower cell parameter. Additionally, a new peak 41.2° forming at 1100°C might belong to the $LaAlO_3$ phase (card #31-22).

In addition to XRD, FTIR analysis of samples was also performed. FTIR allows to see whether the sample contains carbon–oxygen species by detecting their bonds vibrations. Measured spectra are shown in Fig. 8. For the as-deposited sample, strong signals from the C–O bonds are detected. They become smaller after exposure to 500°C and completely vanish after processing at 600°C (the same spectra were obtained for higher processing temperatures). Additionally, annealing at 500°C shows new a C = O band, which confirms the degradation process of polymeric precursor.

By XRD it was shown that the layer crystallizes at 600°C, and from FTIR analysis it can be concluded that at the same temperature the carbonaceous species are removed from the sample. After deposition, the layer contains some leftover C–O and C=O bonds from the solvents used, and processing at 600°C is required to remove them.

Sample microstructures were also analyzed on their polished cross sections. SEM images are presented in Fig. 9. For the as-deposited and 500°C processed layers the adherence of the layer to the sapphire substrate has been weak—a delamination/detachment has been observed. That might be due to epoxy shrinkage during curing—the layers had poor bonding to the substrate and has been pulled off. For the crystallized samples no delamination occurred. Samples processed below 1000°C show similar microstructure with no easily distinguishable grains. At 1000°C and 1100°C larger grains can be observed. New phase formation was detected by XRD at 800°C, but it is not visible by SEM. After processing at 1100°C a reaction between the sapphire and LSC has been observed.

In order to determine the extent of reaction between the sapphire substrate and the LSC layer, EDS analyses of the sample cross sections after

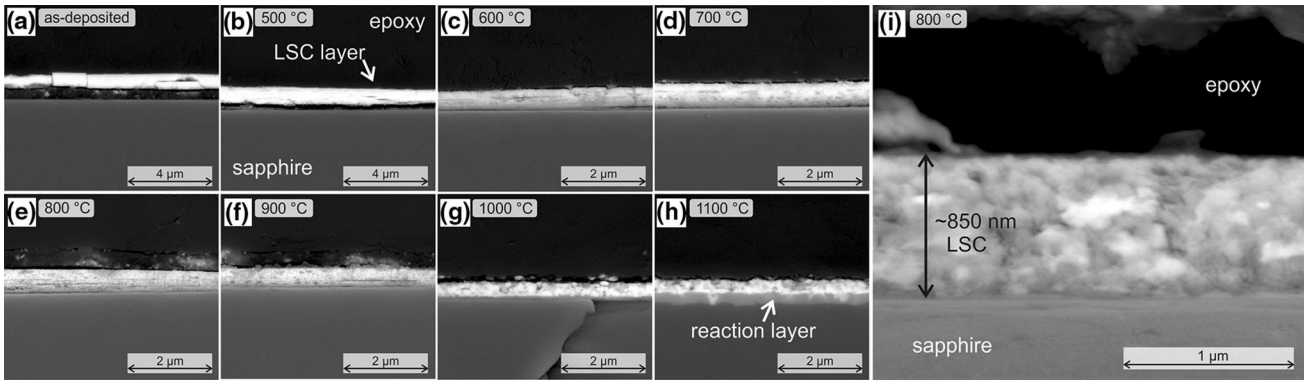

Fig. 9. SEM images of polished cross-sections of LSC films after different heat-treatments as-deposited (a), after: 500°C (b), 600°C (c), 700°C (d), 800°C (e), 900°C (f), 1000°C (g), 1100°C (h) with higher magnification image of the 800°C processed sample (i).

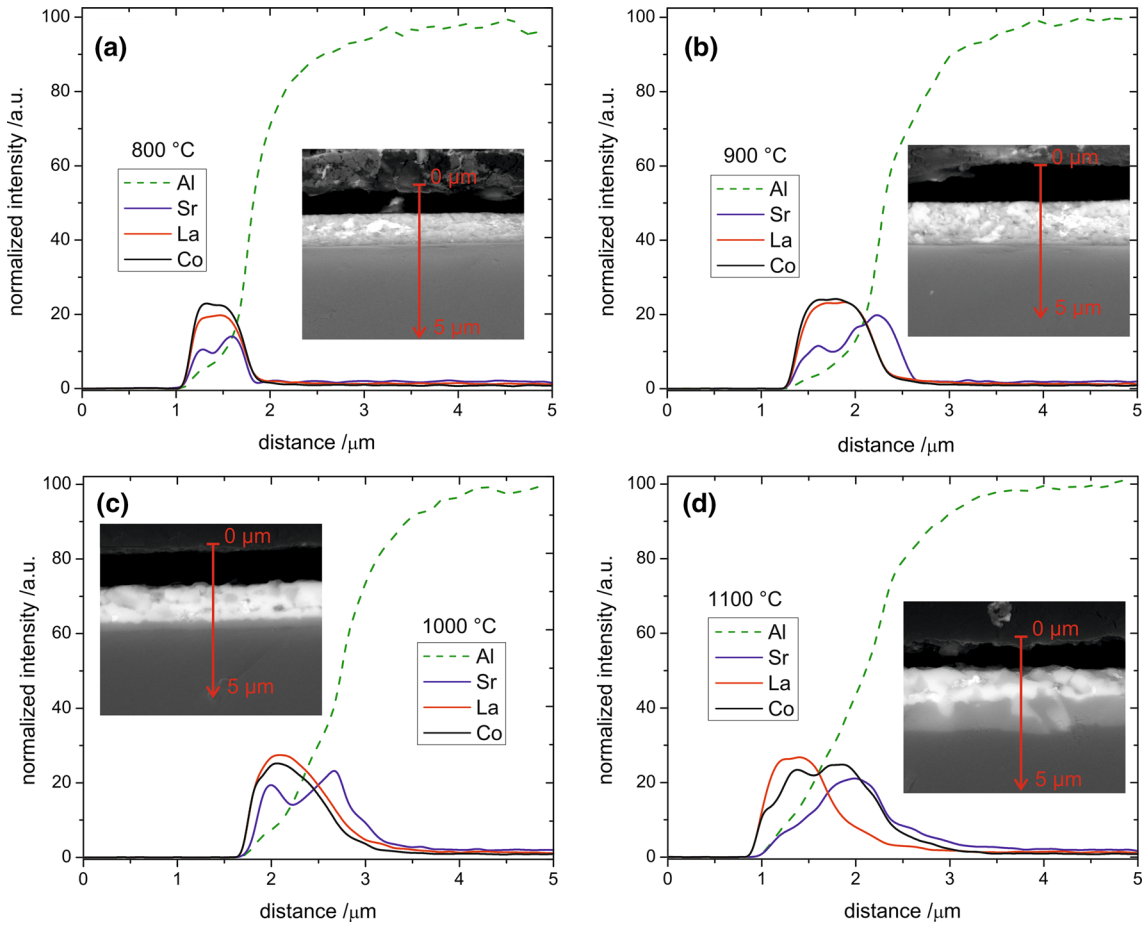

Fig. 10. EDS linescans of layers after heat treatment at 1000°C (a) 900°C (b), 1000°C (c) and 1100°C (d). The insets show the scanning line position across the interface.

exposures at 800°C, 900°C, 1000°C and 1100°C were performed. Results of linescan analysis of Al, Sr, La and Co are shown in Fig. 10a, b, c and d. For the LSC layer annealed at 800°C, a nice narrow profile of the La, Sr and Co cations distribution is visible. There seems to be no interaction with the substrate. For the layer annealed at 900°C, a clear change in Sr distribution is observed. The Sr signal is found in the sapphire substrate. Profiles of La and Co are still contained in the original layer. Even more severe diffusion of Sr is visible for samples after annealing above 900°C. After 1000°C Sr is still present in the LSC layer, but also gives a noticeable signal inside the sapphire substrate. After processing at 1100°C, Sr signal from the LSC layer is not visible, the Sr profile lies inside the sapphire

substrate. Clearly, Sr reacted with sapphire by diffusing into the substrate. To a large extent also Co has reacted with the substrate. It is also possible, that the Al diffused into the initial LSC coating. The profile of the Al signal shows some possible diffusion. Depletion of Sr in the LSC layer leads to the observed unit cell size change (decrease of size) as observed by XRD; however, it does not cause phase change of the LSC material. According to XRD, after even after 1100°C, the LSC still remained as a regular perovskite phase even though most of Sr diffused into the sapphire. In general, it seems that LSC is very active towards a reaction with sapphire, and processing at temperatures exceeding 800°C leads to strong interdiffusion. It might be connected to the reported electrical conductivity maximum, which is found for the sample processed at 800°C and for higher processing temperature it decreases, as presented in Fig. 4. For conductivity data measured during the isothermal holds presented in Fig. 3, gradual decrease of conductivity is observed for annealing at 850°C and higher. This is probably directly connected to the interdiffusion of elements between the LSC layer and the substrates.

In order to describe the observed reactivity of the LSC with sapphire more thoroughly, a phase diagram of the SrO-$AlO_{1.5}$ system was calculated and is presented in Fig. 11. Six complex compounds exist in the studied system: $Al_{12}SrO_{19}$, Al_4SrO_7, low temperature Al_2SrO_4, high temperature Al_2SrO_4, $Al_2Sr_3O_6$, and $Al_{16}Sr_{42}O_{66}$. Alumina can easily react with SrO forming different thermodynamically stable compounds depending on the composition. As determined with the XRD analysis, the compound $Al_2Sr_3O_6$ can form during heating to high temperatures.

MECHANICAL PROPERTIES OF LSC ON SAPPHIRE: ANALYTICAL MODEL

The LSC thin film was deposited on sapphire substrates at 400°C and then annealed at 500–1100°C to stabilize the microstructure and desired properties. Because of a large TEC mismatch, the annealing and subsequent cooling procedure introduces thermal stresses and bending in the bi-layer structure. In the present study, $\Delta T = T_{\text{annealing}} - T_{\text{room}}$, which is used to calculate the biaxial thermal stresses in the examined materials. The elastic properties of the constituent layers used for calculations are listed in Table 3. Shown in Fig. 12a is the stress profile within the sapphire layer after cooling from 800°C to room temperature. A gradual reduction from tensile (in the bottom free surface of the sapphire layer) to compressive stress (close to the interface) was observed. In the coating layer (Fig. 12b), however, a very high constant tensile stress was obtained through its thickness. In practice, though, no delamination and/or cracking was observed in the coating layer. Figure 12c shows the evolved stress within the coating layer after cooling from different annealing temperature. It was seen that the lower annealing temperature is, the lower residual stress is obtained after cooling the sample.

It is worthy to note that in the presence of the temperature dependence of thermal expansion, *E*-

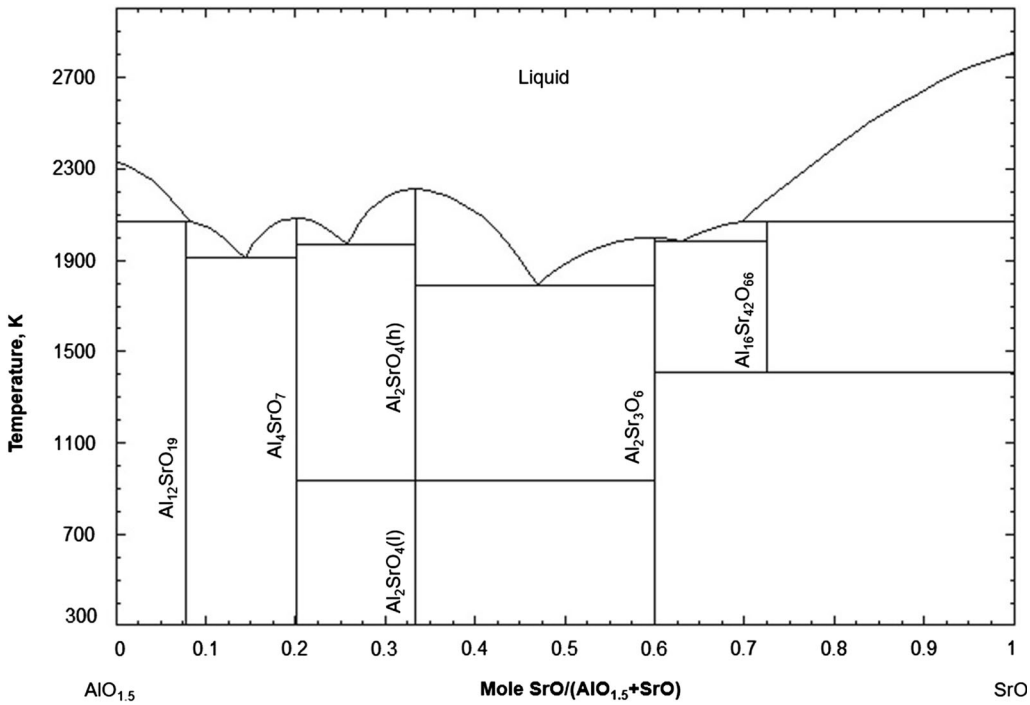

Fig. 11. SrO-$AlO_{1.5}$ phase diagram.

Table III. Thickness and elastic properties of the materials used for calculations

Material/properties	E [GPa]	ν	thickness [μm]	TEC [K^{-1}]
Sapphire (∥ to c-plane)	426	0.31	500	7.7×10^{-6}
LSC	135	0.3	1	20.5×10^{-6}

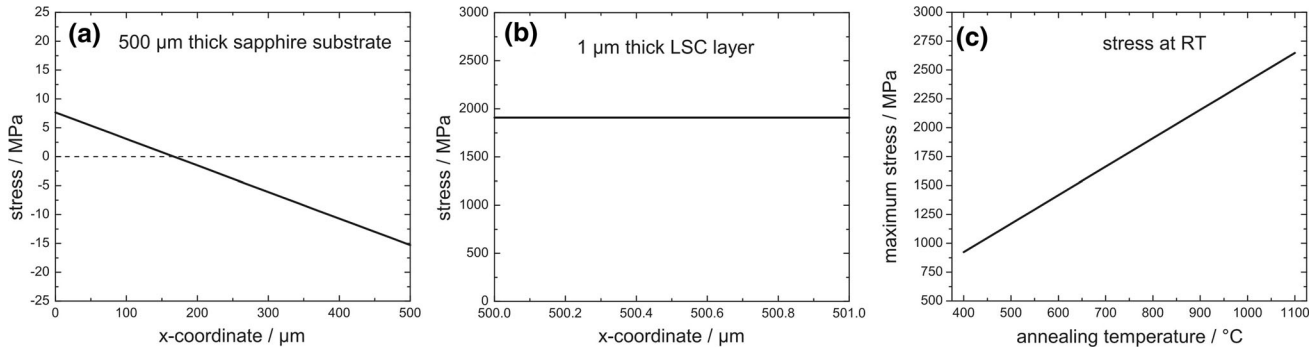

Fig. 12. Calculated stresses developed in the substrate and LSC layer after cooling down from 800°C to room temperature in the sapphire substrate (a), in the LSC layer (b), dependency of maximum stress evolved in LSC layer on the annealing temperature (c).

modulus and Poisson's ratio, the thermal strain should be obtained by replacing an integral of the α, E or ν with respect to the temperature. For this study we used the average α within the temperature range, as well as the average E^* and ν. For LSC material, it has been shown that Young's modulus varies from ~ 135 GPa at room temperature to 130 GPa at 1000°C,[53] which is not significant. Moreover, our calculations, not shown here, showed that the evolved stress is significantly dependent on layer thickness and TEC mismatch of layer and less dependent to difference of Young's modulus and Poisson's ratio. Hence, even if Young's modulus of any layer changes with temperature it doesn't highly influence the stress level within layers.

A very high stress calculated in this work for the LSC layers does not result in visible cracking or delamination of the thin films. Previously, for a similarly deposited $MnCo_{1.6}Cu_{0.4}O_4$ layer on sapphire we have observed cracking due to increased TEC after Cu doping,[54] but the absolute value was still much lower than for the LSC, which is typically regarded as a material with a high TEC (at least among the SOFC materials). One possible explanation for lack of cracking might be that due to interdiffusion between the sapphire and the LSC layer a very strong interface is formed and the properties of the thin layer are modified due to interdiffusion. Future studies will elaborate more on the potential effects of the substrate–layer interactions.

The obtained results can be compared to previous reported research. Several groups have worked with deposition and analysis of LSC thin films with the purpose to utilize them as electrodes in micro-SOFCs. For example, LSC64 thin films were deposited by a very similar spray pyrolysis process by Pecho et al.[55] The authors focused on possible phase composition of the deposited layer, as they have found (by FIB-SEM and TEM) additional strontium phases (either SrO, $Sr(OH)_2$ or $SrCO_3$) in the LSC layer. No electrical conductivity data nor x-ray diffractograms were reported for the films, just its electrochemical performance. Though the deposition process was similar as it utilized gas atomization of liquid precursors into droplets, it utilized a slightly different liquid precursor. Deposition was based on diethyleneglycolmonobutyl ether and PEG600 forming the liquid phase, whereas in our study other solvents and no binder were used. Microstructure obtained in our work seems a bit more compact. In another study, LSC64 layers were deposited by a flame spray pyrolysis process on sapphire substrates and on CGO by Karageorgakis et al.[56] Layers had a thickness of ~ 450 nm, their structural evolution as a function of time and temperature was studied, but no electrical conductivity measurements were reported. Deposited layers were amorphous after the deposition and showed crystalline structure after processing at 600°C. Heat treatment in the temperature range 700–900°C induced visible grain growth and porosity decrease, which in turn led to lowered electrochemical performance. Layers seem to be more porous and rough than the one studied in our work. In other work, Garbayo et al.[57] studied porous LSC64 films deposited by PLD on YSZ and Si-based substrates. The layers had thickness of

350 nm and crystallized in the temperature range of 500–550°C. A maximum electrical conductivity of ca. 300 S cm^{-1} was found for the layers after processing at 700°C.

Based on these reports, our results shows comparable microstructure, but higher electrical conductivity and utilizes a simpler deposition method. Spray pyrolysis seems to be a convenient method for fabrication of thin films with controlled microstructure based on thermal processing.

CONCLUSIONS

In this paper, spray pyrolysis was used to deposit 1 μm thick LSC layers on sapphire substrates. High-quality layers were obtained at $\sim$ 400°C. The deposited layers were initially amorphous. As determined via XRD, they crystallized after exposure at 600°C, which was also associated with the removal of solvent carbon–oxygen residues, as shown by infrared spectroscopy. Structural and compositional analysis revealed the formation of the cubic perovskite phase with the desired cation content. The electrical conductivity of layers exhibited a complex temperature exposure behavior, with a maximum value of $\sim$ 1300 S cm^{-1} achieved after exposure at 800°C. Above 900°C, the diffusion of Sr from the LSC layer into the sapphire was detected. For the film processed at 1100°C, almost all Sr diffused into the sapphire. The phase diagram showed that SrO and $AlO_{1.5}$ formed several thermodynamically stable phases over the whole composition and temperature range.

An analytical model of stress distribution was used to predict the stress occurring in the bi-layer material when cooling it down from the annealing temperature to room temperature. While the maximum principal stresses predicted by the analytical model were found to change slightly in the sapphire substrate, a very high constant tensile stress was predicted within the coating layer, dependent on annealing temperature. Interestingly, the layers did not show any visible cracking or spallation.

The obtained results show that spray pyrolysis is a simple yet efficient process that can be used to deposit complex materials at low temperatures. This makes it possible to study the properties of materials as a function of treatment temperatures from a broad range.

ACKNOWLEDGMENTS

The presented research is part of the "*Nanocrystalline ceramic materials for efficient electrochemical energy conversion*" project, carried out within the First TEAM programme of the Foundation for Polish Science (Grant Agreement Nr. POIR.04.04.00-00-42E9/17-00), co-financed by the European Union under the European Regional Development Fund. Statutory fund of WETI PG is also acknowledged.

OPEN ACCESS

REFERENCES

1. C. Liu, S. Tsai, and C. Ni, *J. Electron. Mater.* 46, 2301 (2017).
2. S.A.M. Solomon, A. George, J. Kumpakkattu, and A. John, *J. Electron. Mater.* 44, 28 (2015).
3. Z.N. Kayani, G. Fatima, B. Zulfiqar, S. Riaz, and S. Naseem, *J. Electron. Mater.* 46, 5764 (2017).
4. M.A. Matin, T. Sugai, N. Kawazu, D. Akai, and K. Sawada, *J. Electron. Mater.* 45, 329 (2016).
5. Y. Chen, Y. Liu, and S. Wang, *J. Electron. Mater.* 47, 3639 (2018).
6. S.V. Rabotkin and V.O. Oskirko, *J. Electron. Mater.* 45, 3921 (2016).
7. H.A. Dehkordi, A.L.I. Mokhtari, K. Dastafkan, and V. Soleimanian, *J. Electron. Mater.* 48, 1258 (2019).
8. T.M. Adams, A.J. Duncan, and J. Fitz-gerald, *J. Electron. Mater.* 34, 2 (2005).
9. L. Filipovic, S. Selberherr, G.C. Mutinati, E. Brunet, S. Steinhauer, K. Anton, J. Teva, J. Kraft, and F. Schrank, *Proc. World Congr. Eng.* II, 6 (2013).
10. Z. Shao, W. Zhou, and Z. Zhu, *Prog. Mater Sci.* 57, 804 (2012).
11. A.P. Jamale, C.H. Bhosale, and L.D. Jadhav, *J. Electron. Mater.* 45, 509 (2016).
12. B. Kamecki, J. Karczewski, T. Miruszewski, G. Jasiński, D. Szymczewska, P. Jasiński, and S. Molin, *J. Eur. Ceram. Soc.* 38, 4576 (2018).
13. L. dos Santos-Gómez, J.M. Porras-Vázquez, E.R. Losilla, F. Martín, J.R. Ramos-Barrado, and D. Marrero-López, *J. Power Sources* 347, 178 (2017).
14. L. Santos-gómez, J.M. Porras-vázquez, E.R. Losilla, F. Martín, and J.R. Ramos-barrado, *J. Eur. Ceram. Soc.* 38, 1647 (2018).
15. J. Will, A. Mitterdorfer, C. Kleinlogel, D. Perednis, and L. Gauckler, *Solid State Ionics* 131, 79 (2000).
16. F. Chiabrera, I. Garbayo, N. Alayo, and A. Tarancón, *Proc. SPIE - Int. Soc. Opt. Eng.* 10246, 102460S (2017). https://doi.org/10.1117/12.2269454.
17. F. Chiabrera, I. Garbayo, and A. Tarancón, *Metal Oxide-Based Thin Film Structures, chap*. 17, ed. N. Pryds and V. Esposito (Elsevier, 2018), pp. 409–439.
18. D. Perednis and L.J. Gauckler, *J. Electroceramics* 14, 103 (2005).
19. T. Terayama, S. Nagata, Y. Tanaka, A. Momma, T. Kato, and M. Kunii, *J. Electron. Mater.* 42, 2306 (2013).
20. I. Garbayo, D. Pla, A. Morata, L. Fonseca, N. Sabaté, and A. Tarancón, *Energy Environ. Sci.* 7, 3617 (2014).
21. R. Barfod, A. Hagen, S. Ramousse, P.V. Hendriksen, and M. Mogensen, *Fuel Cells* 6, 141 (2006).
22. A. Hagen, R. Barfod, P.V. Hendriksen, Y.-L. Liu, and S. Ramousse, *J. Electrochem. Soc.* 153, A1165 (2006).
23. Y. Chen, W. Zhou, D. Ding, M. Liu, F. Ciucci, M. Tade, and Z. Shao, *Adv. Energy Mater.* 5, 1500537 (2015).
24. M. Gazda, P. Jasinski, B. Kusz, B. Bochentyn, K. Gdula-Kasica, T. Lendze, W. Lewandowska-Iwaniak, A. Mielewczyk-Gryn, and S. Molin, *Solid State Phenom.* 183, 65 (2012).
25. C. Sun, R. Hui, and J. Roller, *J. Solid State Electrochem.* 14, 1125 (2009).

26. Y. Tao, J. Shao, J. Wang, and W.G. Wang, *J. Power Sources* 185, 609 (2008).
27. P. Hjalmarsson, M. Søgaard, and M. Mogensen, *Solid State Ionics* 179, 1422 (2008).
28. J. Hayd, H. Yokokawa, and E. Ivers-Tiffee, *J. Electrochem. Soc.* 160, F351 (2013).
29. W.C. Chueh and S.M. Haile, *Annu. Rev. Chem. Biomol. Eng.* 3, 313 (2012).
30. J.T.S. Irvine, D. Neagu, M.C. Verbraeken, C. Chatzichristodoulou, C. Graves, and M.B. Mogensen, *Nat. Energy* 1, 15014 (2016).
31. H. Ullmann, N. Trofimenko, F. Tietz, and D. Stover, *Solid State Ionics* 138, 79 (2000).
32. A.J. Jacobson, *Chem. Mater.* 22, 660 (2010).
33. Y. Zhang-Steenwinkel, Q. Yu, F.P.F. van Berkel, M.M.A. van Tuel, B. Rietveld, and H. Tu, *Int. J. Hydrogen Energy* 41, 5824 (2016).
34. A.J. Samson, P. Hjalmarsson, M. Søgaard, J. Hjelm, and N. Bonanos, *J. Power Sources* 216, 124 (2012).
35. A.J. Samson, M. Søgaard, P. Hjalmarsson, J. Hjelm, N. Bonanos, S.P.V. Foghmoes, and T. Ramos, *Fuel Cells* 13, 511 (2013).
36. S. Molin and P.Z. Jasinski, *Mater. Lett.* 189, 252 (2017).
37. L. Zhang, L. Zhu, and A.V. Virkar, *J. Electrochem. Soc.* 163, F1358 (2016).
38. N. Hildenbrand, B.A. Boukamp, P. Nammensma, and D.H.A. Blank, *Solid State Ionics* 192, 12 (2011).
39. S. Choi, C.J. Kucharczyk, Y. Liang, X. Zhang, I. Takeuchi, H.-I. Ji, and S.M. Haile, *Nat. Energy* 3, 202 (2018).
40. C.W. Bale, P. Chartrand, S.A. Degterov, G. Eriksson, K. Hack, R. Ben Mahfoud, J. Melançon, A.D. Pelton, and S. Petersen, *Calphad* 26, 189 (2002).
41. C. Hsueh, C.R. Luttrell, and T. Cui, *J. Micromech. Microeng.* 16, 2509 (2006).
42. C. Hsueh, *J. Appl. Phys.* 91, 9652 (2002).
43. D. Beckel, A. Dubach, A.R. Studart, and L.J. Gauckler, *J. Electroceramics* 16, 221 (2006).
44. A.N. Petrov, O.F. Kononchuk, A.V. Andreev, V.A. Cherepanov, and P. Kofstad, *Solid State Ionics* 2738, 189 (1995).
45. M. Kubicek, G.M. Rupp, S. Huber, A. Penn, A.K. Opitz, J. Bernardi, M. Sto, and H. Hutter, *Phys. Chem. Chem. Phys.* 16, 2715 (2014).
46. Đ. Tripković, R. Küngas, M. Mogensen, and P.V. Hendriksen, *J. Mater. Chem. A* 7, 11782 (2019).
47. M. Mosleh and N. Pryds, *PV Hendriksen* 144, 38 (2017).
48. P. Plonczak, D.R. Sørensen, M. Søgaard, V. Esposito, and P.V. Hendriksen, *Solid State Ionics* 217, 54 (2012).
49. P. Plonczak, A. Bieberle-Huetter, M. Sogaard, T. Ryll, J. Martynczuk, P.V. Hendriksen, and L.J. Gauckler, *Adv. Funct. Mater.* 21, 2764 (2011).
50. A.A. Samat, A.A. Jais, M.R. Somalu, N. Osman, A. Muchtar, and K.L. Lim, *J. Sol–Gel Sci Tech* 86, 617 (2018).
51. G.M. Rupp, H. Tellez, J. Druce, A. Limbeck, T. Ishihara, J.A. Kilner, and J. Fleig, *J. Mater. Chem. A* 3, 22759 (2015).
52. C. Link, A.K. Opitz, C. Rameshan, M. Kubicek, G.M. Rupp, and A. Nenning, *Top. Catal.* 61, 2129 (2019).
53. H. Bingxin, *Thermo-Mechanical Properties of Mixed Ion-Electron Conducting Membrane Materials*, RWTH Aachen (2010).
54. D. Szymczewska, S. Molin, P. Hendriksen, and P. Jasiński, *Cryst.* 7, 185 (2017).
55. J. Martynczuk, T. Hocker, O. Pecho, L. Holzer, R.J. Flatt, and M. Prestat, *J. Power Sources* 274, 295 (2015).
56. N.I. Karageorgakis, A. Heel, A. Bieberle-hütter, J.L.M. Rupp, T. Graule, and L.J. Gauckler, *J. Power Sources* 195, 8152 (2010).
57. I. Garbayo, V. Esposito, S. Sanna, A. Morata, D. Pla, L. Fonseca, N. Sabaté, and A. Tarancón, *J. Power Sources* 248, 1042 (2014).